Austenite Formation during Laser Surface Hardening of Fully Pearlitic Steel

Castro Cerda, Felipe; Sepúlveda, Estefanía; Kestens, Leo; Wood, G.; Méndez, Patricio

DOI
10.1002/srin.202500747

Publication date
2025

Document Version
Final published version

Published in
Steel Research International

steel research international
www.steel-research.de

Austenite Formation during Laser Surface Hardening of Fully Pearlitic Steel

Felipe Castro Cerda, Estefanía Sepúlveda, Leo Kestens, Gentry Wood, and Patricio Méndez*

Despite the widespread use of laser heat treatment, a fundamental understanding of austenite formation kinetics at high heating rates remains a challenge. This gap is addressed by developing a novel model that uniquely accounts for the initial pearlite colony size and interlamellar spacing as critical input parameters. The model's predictions are validated against experimental observations, where the spatial variation of hardness reveals a distinct two-zone microstructure: a fully austenitized region and a partially transformed intercritical layer. The results show that the relative size of these zones is directly controlled by the initial microstructure. This research provides a crucial insight that austenite formation under rapid heating conditions occurs with negligible superheating, which is essential for optimizing laser processing parameters to achieve a desired microstructure.

1. Introduction

Laser heat treatments (LHT) represent a reliable technological strategy for improving the surface properties of steel, primarily due to two practical reasons: enhanced surface quality and a strong potential for automatization. Under proper control conditions, LHT can produce high-quality surface parts with virtually no further processing steps. While several reviews have summarized the advantages and main features of LHT,[1–6] they have not adequately addressed the importance of the initial microstructure as a design parameter. This article addresses that gap by presenting a novel model for austenite formation that uniquely includes the influence of nodule size and interlamellar spacing, which are critical variables for accurately predicting the final properties of laser-treated steel.

There are few examples in the literature that attempt to introduce the microstructure as a variable for predicting the final properties of LHT steel parts. Martínez et al.[7] developed an empirical model to predict hardness after laser heat treatment in DINCk45 steel. While this model is based on determining the martensite fraction after the thermal cycle, its applicability is limited because it requires the parameters of the JMAK equation to be determined through separate dilatometric studies. The problem of modelling the phase transformations in a pearlitic structure under a laser beam has been originally treated by Ashby and Easterling.[8] In their work, they considered two hypo-eutectoid steels of ferrite and pearlite initial microstructure, whereby, the formation of austenite (γ) is parameterized by the sidewise dissolution of a cementite (θ) plate. They further proposed that the formation of austenite during heating should be subject to considerable overheating due to the lengthwise dissolution of cementite, which is correlated with the colony size. Surprisingly, these microstructural parameters were subsequently neglected in their model by stating that pearlite is instantaneously dissolved into austenite of the same carbon content. Further modelling efforts of the laser heat treatment of pearlitic steels[9–14] seem to have accepted the microstructural approach by Ashby and Easterling,[8] focusing more in the numerical development of the thermal profiles. However, no consistent revision of the actual role of pearlite during austenite formation in original model have been attempted until recently,[15] whereby it was shown that the kinetics of cementite dissolution is one important factor affecting the carbon content of austenite during LHT. Cast irons of pearlitic[16,17] and pearlitic-bainitic[18] microstructures, and a variety of low-alloyed steels,[19–23] have used pearlitic or ferritic-pearlitic initial microstructures for laser surface hardening

F. Castro Cerda, E. Sepúlveda
Department of Metallurgy
University of Santiago de Chile
Alameda Bdo. O'Higgins 3363, Santiago 9170022, Chile
E-mail: felipe.castro@usach.cl

E. Sepúlveda, L. Kestens
Department of Electromechanical
Systems and Metal Engineering
Ghent University
Technologiepark 46, Ghent B-9052, Belgium

L. Kestens
Department of Mechanical
Maritime and Materials Engineering
Delft University of Technology
Mekelweg 2, Delft 2628 CD, The Nederlands

G. Wood
Apollo-Clad Laser Cladding
Apollo-Machine and Welding Ltd
4112 91A Street NW, Edmonton, AB T6E 5V2, Canada

P. Méndez
Department of Chemical and Materials Engineering
Donadeo Innovation Centre for Engineering
University of Alberta
9211 116 Street NW, Edmonton T6G 1H9, Canada

The ORCID identification number(s) for the author(s) of this article can be found under https://doi.org/10.1002/srin.202500747.

DOI: 10.1002/srin.202500747

experiments. However, no quantitative correlation between the microstructural parameters of pearlite, laser processing parameters, and the characteristics of the hardness layer is proposed.

Uncoupled cementite dissolution models deliver predictions of microstructural evolution that may not be compliant with experimental observations. One possible shortcoming is the erroneous prediction of carbon enrichment in austenite, therefore an incorrect estimation of the hardness of martensite. Additionally, the impact of the pearlitic nodule size on the microstructure after laser heat treatment has not yet been assessed or implemented in a model. Consequently, the aim of the present study is to propose a model to evaluate the formation of austenite and the final hardness in steel of fully pearlitic initial microstructure after LHT. Due to their significance for the final properties of the hardened layer, the model highlights two novel aspects: 1) the parameters implemented to describe the microstructure are the nodule size and the interlamellar spacing and 2) the coupling of cementite dissolution and carbon redistribution in austenite. The model is validated using an AISI 1095 reference alloy and in-depth microstructural characterization techniques such as high-resolution scanning electron microscopy (SEM), electron backscattered diffraction (EBSD), and Vickers hardness profiles.

2. Model Development

2.1. Nucleation and Growth of Austenite

The laser beam produces thermal gradients that have been described in a previous work.[24] The peak temperature T_{peak} (K) for a given depth z (m) in the sample under a laser beam moving with a velocity U (ms^{-1}) is given by

$$T_{Peak} = T_0 + \frac{2\eta q}{\sqrt{\pi}k}\sqrt{\frac{\alpha}{UW^3}} - \frac{\eta q}{W^2 k}z \tag{1}$$

where q is the beam power in (J s^{-1}), η is the thermal efficiency of the process, k is the thermal conductivity of the substrate in (J s^{-1} m^{-1} K^{-1}), α is the thermal diffusivity of the substrate in (m^2 s^{-1}), T_0 is the starting or preheat temperature (K), W is the side of the square shape projected by the laser beam in (m), and z is depth under the surface in (m).

Ashby and Easterling[8] proposed that the extent of a diffusion-controlled transformation will be equivalent to the average number of atomic jumps at a given temperature and time. In an isothermal process, the extent of a transformation is proportional to the quantity $\sqrt{Dt}$, where D is the diffusivity in m^2 s^{-1} and t is the time in s. In a thermal cycle such as laser heat-treatments, the temperature evolution was approximated by them as parabolic. Using this approach, Ashby and Easterling[8] defined an integrated quantity called "kinetic strength" as a function of the peak temperature, which is equivalent to

$$I = 3\tau\sqrt{\frac{RT_{Peak}}{Q}}\exp\left(-\frac{Q}{RT_{Peak}}\right) \tag{2}$$

where Q is the activation energy of the diffusional process in (J mol^{-1}), R is the gas constant in (J m^{-1} K^{-1}), and τ is the thermal time constant related to the amplitude of the temperature cycle. For cases of short resident times (W U^{-1}), τ can be estimated as

$$\tau = \frac{\left(\frac{\eta q}{UW}\right)^2}{\pi^2 e c_v (T_{Peak} - T_0)^2} \tag{3}$$

where c_v is the heat capacity at constant volume in (J m^{-3} K^{-1}). The kinetic strength has units of time and accounts for a time-varying diffusivity by replacing the ubiquitous quantity Dt in diffusion processes for $D_0 I$.

Under the assumption that the nucleation stage begins immediately above A_1, the formation of austenite in a pearlitic initial microstructure can be thought of as a process in which a thin film of austenite grows towards ferrite and cementite. Experimental observations[25] suggest that ferrite dissolves relatively faster than cementite under rapid heating conditions. This is mainly due to the system evolving to a temperature range where the γ to α reaction is interface-controlled. Conversely, cementite dissolution is always carbon diffusion controlled, since carbon must be transported away from the θ/γ interface. Therefore, the original ferrite and cementite microstructure would quickly evolve to an austenite and cementite mixture. The diffusion distance of carbon in austenite growing toward cementite could be approached by one half of the average interlamellar distance S (m). This hypothetical case would yield an expression for the fast isothermal growth of austenite of the type $S^2 = 4Dt$, where the time for completion depends only on the interlamellar spacing, as originally proposed by Ashby and Easterling.[8]

The growth of austenite into pearlite has been documented to begin primarily on the boundaries between nodules.[26] Supposing that this fast nucleation stage is represented by a thin film of austenite which covers the area of a pearlite nodule, the kinetic expression of the isothermal spherical growth of austenite would be given by

$$r_\gamma = \frac{4Dt}{S} \tag{4}$$

where r_γ is the radius of the representative austenite grain. Equation (4) can describe a case in which the process of isothermal austenite formation is still kinetically governed by a constant growth rate, inversely proportional to the interlamellar spacing S. The interlamellar spacing is experimentally measured as the sum of the half thickness of ferrite and cementite plates. In a fully pearlitic microstructure, the austenite volume fraction f_γ would therefore be expressed as

$$f_\gamma = \left(\frac{r_\gamma}{r_P}\right)^3 \tag{5}$$

where r_P is the representative radius of pearlitic nodules. To describe the continuous heating of a fully pearlitic sample, the isothermal kinetics was treated as in provided in Refs. [8,15,24] by using the "kinetic strength" I of the thermal cycle.

Combining Equation (6) with Equation (5) and Equation (4), the expression that describes the formation of austenite in a laser cycle is

$$f_\gamma = \left[12\frac{D_0\tau}{r_P S}\sqrt{\frac{RT_{\text{Peak}}}{Q}}\exp\left(-\frac{Q}{RT_{\text{Peak}}}\right)\right]^3 \quad (6)$$

2.2. Dissolution of Cementite

Cementite dissolution has been previously treated as a linearized gradient problem,[27] whereby cementite is in contact with austenite of the same chemical composition as pearlitic ferrite. This model delivers kinetics of cementite dissolution in austenite initially fast,[15,24] yet decreasing with time as typically of parabolic solutions. The present work proposes that the dissolution of cementite is limited by the maximum amount of C in austenite, that is, the solvus line. This approach is implemented by calculating f_γ as first step and then estimating the maximum fraction of cementite in equilibrium with austenite at the step, $f_\theta^{\max}$ as the result of the mass balance of C

$$f_\theta^{\max} = \frac{w_0 - w_C^{\gamma/\theta} f_\gamma}{w_C^\theta} \quad (7)$$

where $w_i^{j/k}$ is the mass fraction of i in the phase j in equilibrium with k, w_0 is the initial mass fraction of carbon, and w_C^θ is mass fraction of carbon in cementite. $w_C^{\gamma/\theta}$ corresponds to the value given by the γ/θ solvus line. For the present study, a linearization is expressed as

$$w_C^{\gamma/\theta} = 0.003115\,T - 1.459194 \quad (8)$$

where the temperature T is in K.

2.3. Hardness of Martensite

In the present study, it was considered that the predicted fraction of austenite will transform completely into martensite. The hardness of martensite H_M is calculated according to the following equation

$$H_M = -926(w_C^\gamma)^2 + 1996 w_C^\gamma + 150 \quad (9)$$

Whereas the average hardness H of the microstructure is estimated by

$$H = f_\gamma H_M + (1 - f_\gamma) H_P \quad (10)$$

where H_P is the average hardness of pearlite. The value of other ancillary parameters used in the calculations is summarized in **Table 1**.

3. Experiment

The material selected for this study corresponds to an AISI 1095 steel. The nominal chemical composition is given in **Table 2**.

Table 1. Input parameters for the model.

Parameter	Value	Unit
η	0.7	–
W	$14.5\,10^{-3}$	m
L	$14.5\,10^{-3}$	m
q	3030	$J\,s^{-1}$
U	0.003654	$m\,s^{-1}$
$k^{a)}$	37	$W\,m^{-1}\,K^{-1}$
$\alpha^{a)}$	$6.35\,10^{-6}$	$m^2\,s^{-1}$
$c_v{}^{a)}$	$4.5\,10^6$	$J\,m^{-3}\,K^{-1}$
T_0	365	K
D_0^γ	10^{-5}	$m\,s^{-1}$
Q^γ	$135\,10^3$	$J\,mol^{-1}$
w_0	0.95	wt%
w_C^θ	6.68	wt%
H_P	331	HV

[a)]Calculated using Thermo-Calc (database TCFE12) and the methodology described in Ref. [31].

Table 2. Chemical composition of substrate (wt%).

C	Mn	Si	S	P
0.95	0.40	0.20	0.02	0.05

3.1. Laser Heat Treating

The experimental set-up is similar to the used in previous experiments.[15,24] Laser heat treatment of the test samples was conducted using a 6 kW YLS-6000 IPG laser integrated with 4-axis CNC motion control system. A 600 µm fiber connected the IPG laser to the Precitec laser heat treat optics.

The optics were comprised of a 150 mm collimation lens, 200 mm ZnS MS faceted focusing lens, and disposable fused quartz protective coverslide at the end of the optics stack. The net effect of the optics configuration was to establish a square laser spot at the sample surface at a working distance of 178 mm (7 in.) above the substrate.

The laser spot size was calibrated using a PRIMES BM60+ laser beam profiler. The laser power delivered to the workpiece was verified using a 10K-W-BB-45-V3 laser power meter from OPHIR Photonics.

The laser test parameters were the following: spot size (W): 13 mm, laser power (q): 3.03 kW, thermal efficiency (η): 0.7, and travel speed (U): $3.654\,10^{-3}\,ms^{-1}$. All test parameters were held constant for all laser heat treatment procedures to isolate the effect of substrate chemistry and initial microstructure on the resulting phase transformations.

Prior to laser heat treatment, the test samples were surface ground to an Ra 0.4 µm surface finish to remove any irregularities that could influence laser absorption. The samples were degreased with acetone, coated with a thin layer of flat black enamel paint, and one laser heat pass of 150 mm long was completed.

4. Characterization Techniques

Specimens for microstructural observation were cut in the same plane previously described. The procedure was the standard grinding and polishing to 1 μm diamond paste. The specimens were etched with Nital 2 vol. percent for four seconds. Optical microscopy was performed in a Keyence optical microscope model VHX-7000, under bright field illumination mode.

For SEM and EBSD analyses, a FEI Quanta 450-FEG-SEM equipped with a Hikari EBSD camera. The SEM was operated at an accelerating voltage of 20 kV and a beam current of 2.3 nA. The scan covered an area of $64 \times 128\ \mu m^2$, with a step size of 0.1 μm. The post-processing of the data was carried out with OIM Software version 8. The post-processing of the EBSD data consisted only in stripping out the points with a confidence index ≤ 0.1. The grain definition adopted in the present study corresponds to a minimum of two points in different rows, with a tolerance angle of 5°. Pearlitic interlamellar spacing S was determined using the linear intercept method on SEM images at 50.000x. Several lines were drawn orthogonal to the pearlitic plates in regios where the orientation of the plates looked normal to the plane of observation. Pearlitic nodule radius r_γ was determined from EBSD scans in the base material, considering only high angle grain boundaries (misorientation $> 15°$). The measured microstructural parameters for the present steel are listed in **Table 3**.

Vickers hardness tests were carried out in a plane transversal to the beam direction, along a straight line coincident with the centerline and mid-length of the heat treatment pass. The applied load was 200 gf for 15 s.

5. Description of Microstructure

Figure 1 shows the microstructure of the studied steel at different magnifications. Figure 1g displays a low magnification image of a region near the surface of the sample, where three distinctive zones are readily visible. The upper side corresponds to the hardened layer and consist mostly of martensite. Figure 1a,b shows high resolution images of this layer in a zone within the hardened layer, in which it is shown that the dissolution of cementite is not complete. The lower side corresponds to the base material, in this case a fully pearlitic microstructure. Pearlite is clearly resolved in the high-resolution images of Figure 1e,f. The transition zone between the upper and lower ends consists of martensite and partially dissolved pearlite. Figure 1c,d shows a grain of austenite (martensite, green arrow) in an early stage of growth.

EBSD maps of the transition zone are shown in **Figure 2**. The area from where the scan was taken is denoted as a black dashed rectangle in Figure 1g. Image quality (IQ) map (Figure 2a) displays the typical contrast between bright areas and dark areas which is associated with a decreasing quality pattern. This has been interpreted elsewhere[28] as an indication of relatively defect-free (pearlite) and distorted (martensite) areas. The refinement of the microstructure towards the surface of the sample is observed in the unique grain color (UGC) map. Large grains at the bottom of the sample, which look bright in the IQ map, are associated with pearlitic nodules, whereas small grains are associated with martensite. Figure 2c shows the Kernel average misorientation (KAM) map, which represents by a color code the misorientation angle between two first neighbors. It is observed that there are clearly high KAM regions across the transition zone, although what was identified as pearlite seems to have low KAM values.

Figure 3a shows a zoomed in section of the EBSD map of Figure 2c where pearlitic nodules are of a larger size than martensite grains (bottom of the image). It can be clearly seen that the large grains, outlined by black lines, are mostly blue (which indicates small crystal rotation). Martensitic grains are mostly light green to red, and it seems that they are clustered in between large grains. It is also observed in the inverse pole figure (IPF) map of Figure 3b that some small grains of low KAM values (white arrows) have the same crystal orientation (black arrows), which is represented by same color in Figure 1b. This type of microstructure suggests a phase distribution like what is shown in Figure 1c,d.

Table 3. Microstructural parameters.

Parameter	Value (SD)	Unit
S	0.32 (0.06)	μm
r_γ	12.4 (5.3)	μm

6. Discussion

The results of the model are displayed in **Figure 4**, which present values for a constant interlamellar spacing $S = 0.1$ μm (Figure 4a, c,e,g) and constant pearlitic nodule radius $r_\gamma = 30$ μm (Figure 4b, d,f,h). Both parameters modify the fraction of transformed austenite f_γ in Equation (6), thereby the hardness according to Equation (10). The experimental hardness measurements are denoted by squares in Figure 4a,b. Solid lines represent the depth variation of hardness values as a function of the radius of the nodule (r_P) in Figure 4a, whereas, Figure 4b shows the same for different values of the interlamellar spacing (S). Both figures indicate that there is a marked difference in the depth of the hardened layer as a function both variables. Figure 4c,d shows the evolution of the fraction of austenite f_γ as a function of r_P and S. As readily shown in Equation (7), f_γ is inversely proportional to r_P and S, which predicts a large fraction of small pearlitic nodules or interlamellar spacings. Figure 4e,f shows the depth variation of the carbon content of austenite (W_C^γ) as a function of r_P and S. The carbon enrichment in austenite becomes more significant as r_P and S increase, yet with no significant increase in the average hardness. Figure 4g,h shows the depth variation of the fraction of cementite f_θ as a function of r_P and S. It is noteworthy that as both r_P and S increase, significant values of f_θ are predicted near the surface of the specimen.

6.1. Microstructure Evolution

High magnification SEM images in Figure 1a,b show that carbides are present in the microstructure, which is due to the

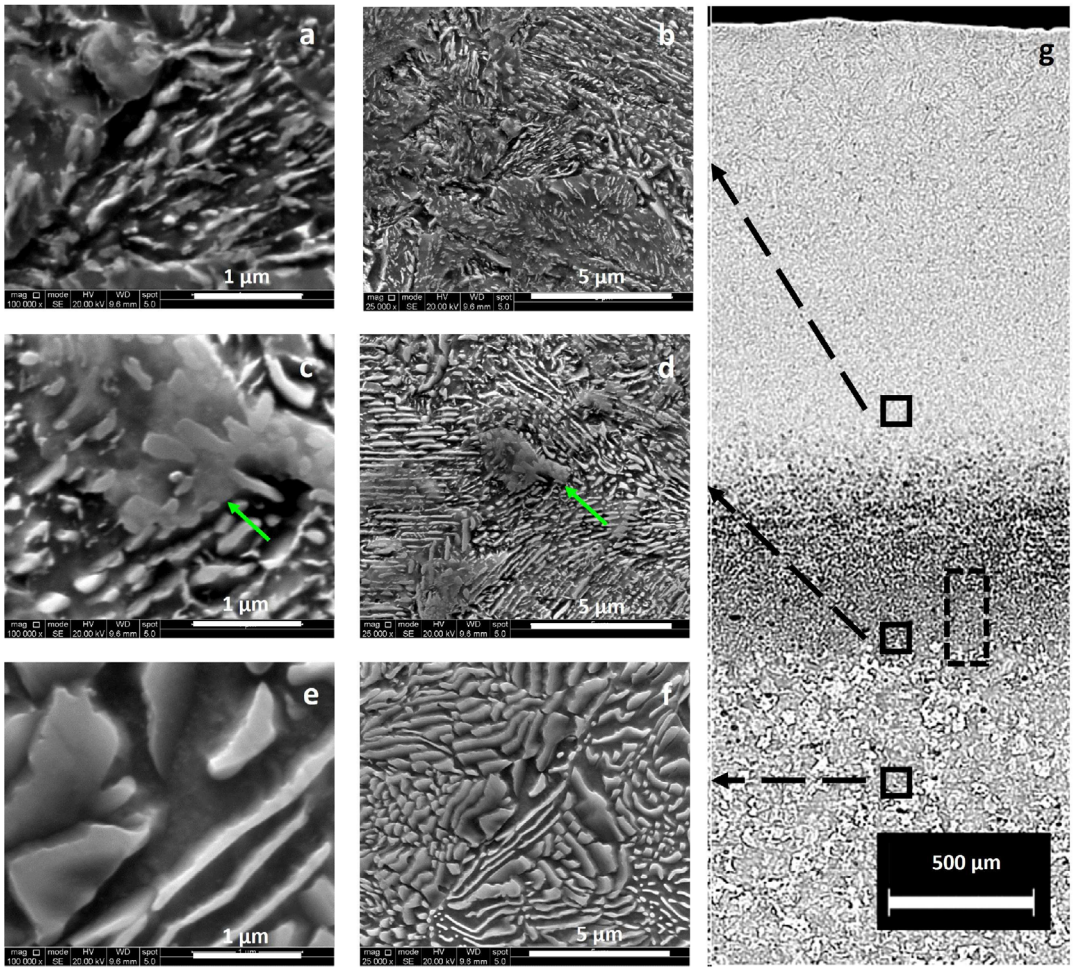

Figure 1. Microstructure of the laser heat treated sample. a–f) correspond to high magnification SEM images, whereas g) is a low magnification micrograph obtained with optical microscopy. Black squares denote the areas from where high resolution images were taken. Dashed black rectangle indicates the area of the EBSD scan.

incomplete dissolution of pearlite. Figure 1c,d shows a region where austenite nucleated and started to grow. Since this region corresponds to new grains, the transition zone displays a fine grain size (cf. Figure 2a,b). The newly grown grains of austenite will transform into martensite on cooling, which will create zones of large KAM due to the distortion associated with the martensitic transformation (Figure 1c). These regions are clearly highlighted in Figure 3a as green-red zones.

It is possible that one austenite grain may deliver martensitic grains with several different orientation variants according to the original γ/α orientation relationship. The presence of small grains between large pearlitic nodules (lower-right corner of Figure 3a,b) suggests that the preferent nucleation sites of austenite are the boundaries between pearlitic nodules.

The onset of austenite formation, A_1 temperature, is achieved under the present laser parameters at a depth value of ≈2 mm. This temperature seems to correspond to the change in the slope of hardness from the base material to the transition zone (Figure 4a). This may suggest that the onset of the formation of austenite in LHT correspond to the A_1 temperature, or a negligible overheating. The observation in the present study contrasts with the general picture[8,29] that austenite formation in fast heating experiments is associated with a large overheating.

6.2. Validation of the Model

The evolution of austenite fraction as a function of the depth is shown in Figure 4c,d for different values of r_P and S, respectively. As predicted by Equation (6), small values of these parameters predict a fast formation of austenite. Hence, small values of r_P and S should produce the largest depth in the hardened layer, as shown by the red curves in Figure 4a,b. This is due to the short times involved in both austenite growth and cementite dissolution (Figure 4g,h). Conversely, large values of r_P and S will extend the transition zone, reducing the depth of the hardened layer (blue curves in Figure 4a,b).

The effect of r_P on the cementite fraction (and in the C content of austenite) is due to the coupling effect expressed in Equation (7). The maximum carbon content that can be stored in austenite $W_C^{\gamma/\theta}$ is given by the γ/θ solvus line at a specific temperature, as expressed in Equation (8). The model simplifies the

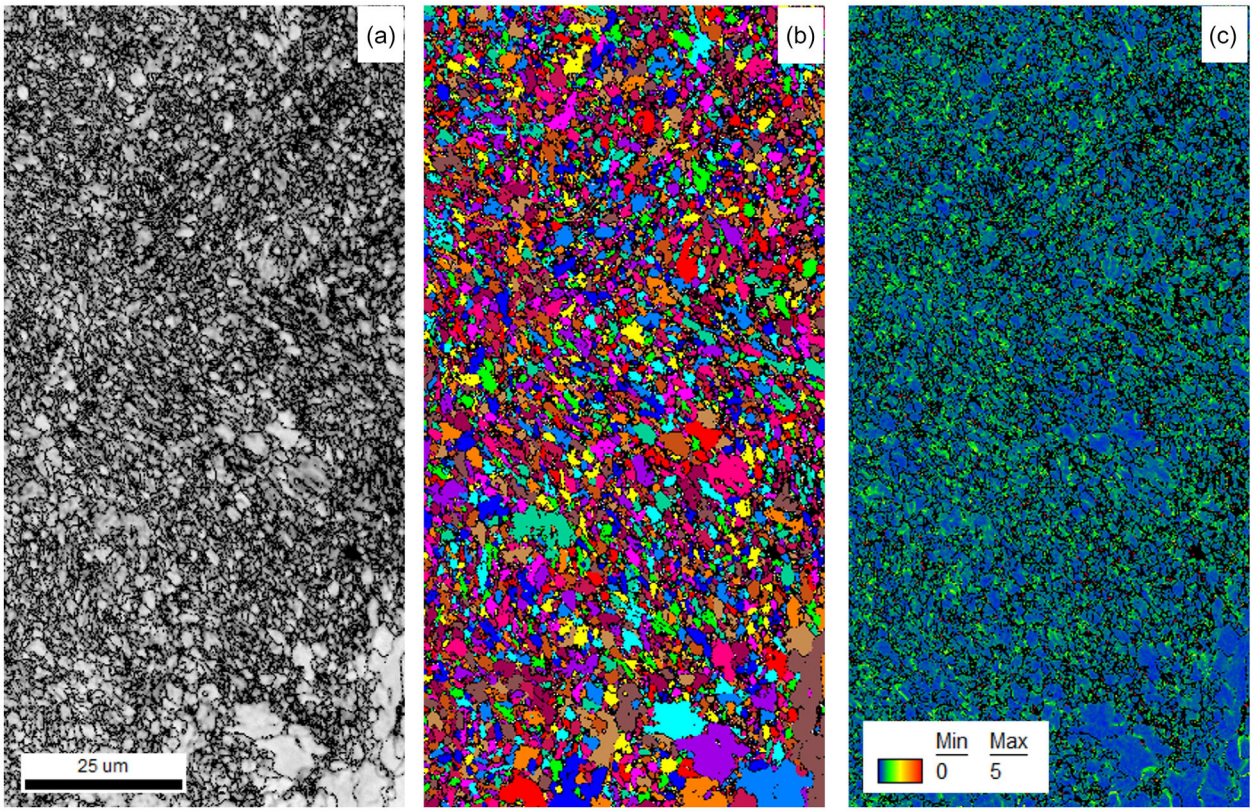

Figure 2. EBSD based maps of the transition zone. a–c) correspond to IQ, UGC, and KAM maps, respectively. Black lines denote high angle grain boundaries.

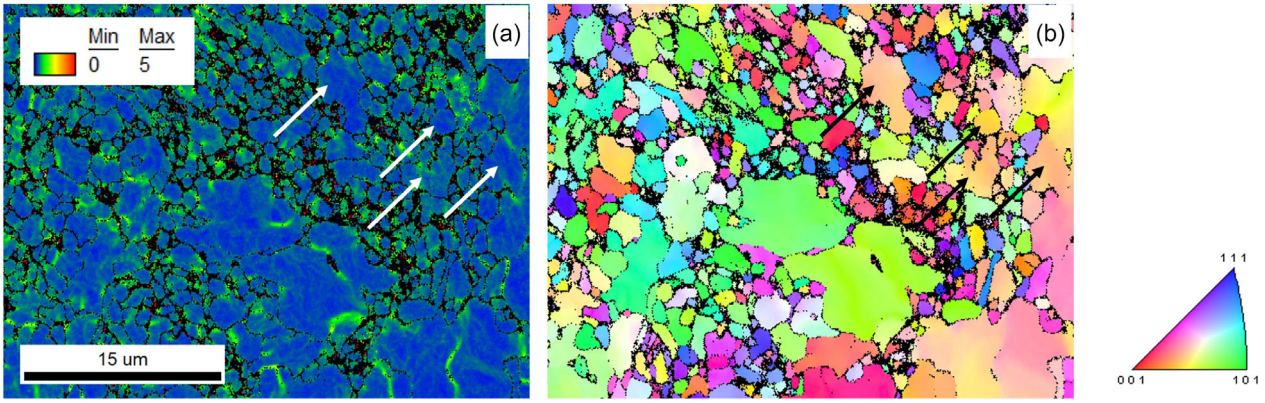

Figure 3. EBSD-based maps of the transition zone. a,b) correspond to KAM and IPF maps, respectively. Black lines denote high angle grain boundaries.

rather complex dynamic carbon profile that establishes between cementite and austenite by assuming that the maximum value of $W_C^{\gamma/\theta}$ is dissolved in austenite at any temperature. Since most of the models implemented in predictions of austenite formation in LHT predict a fast uncoupled dissolution of cementite,[8,15,24,30] the coupling of austenite fraction (Equation 6) and carbon dissolution (Equation 8) will prevent cementite to dissolve beyond its equilibrium fraction (Equation 7). This is clearly seen in Figure 4g, which establishes a correlation between the fraction of cementite dissolved and f_γ for different values of r_P. These two parameters should not be dependent on each other in an uncoupled model. Figure 4f shows the correlation between the interlamellar spacing and the fraction of cementite, which is calculated from Equation (7). According to the present model, coarse interlamellar spacing will reduce the kinetics of austenite formation and increase the carbon content in austenite.

The predictions of hardness are principally influenced by the fraction of austenite. The maximum value is found to occur for 100% of formation and correspond to the prediction of

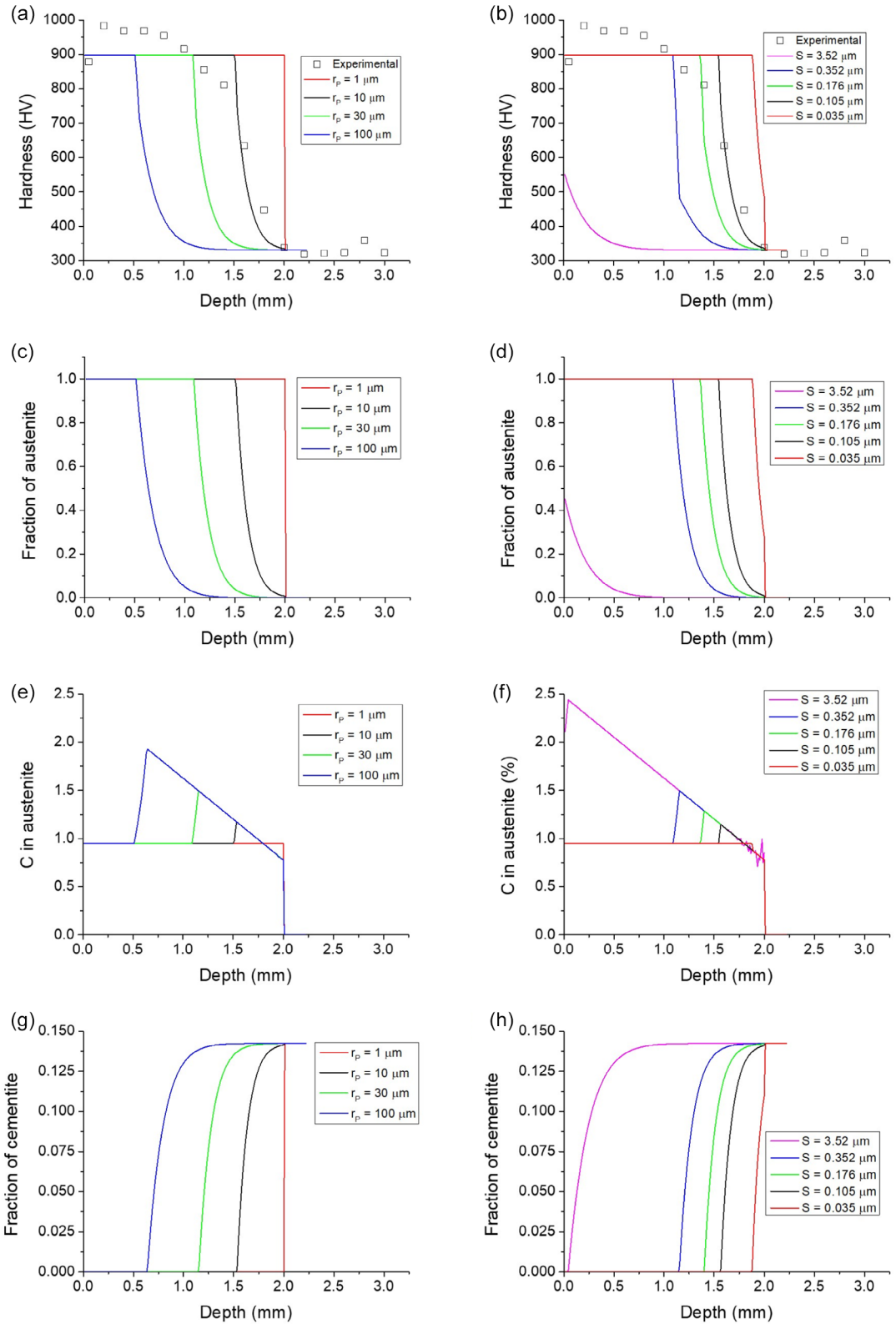

Figure 4. Depth variation of several calculated variables as a function of a,c,e,g) the nodule radius r_P and b,d,f,h) interlamellar spacing S.

Equation (10). This value (898 HV) shows a good agreement with the experimental value of hardness near the surface (878 HV).

There is a discrepancy between the hardness predictions of Equation (10) and the experimental values at depths between 0.2 and 1 mm in the fully austenized hardened layer. The reason for this discrepancy is not yet fully understood, although it has been reported elsewhere[15,24] and seems to be a typical phenomenon in LHT.[1] The difference between predicted and experimental values seems to be more pronounced as the carbon content of the steel increases. This could be interpreted as a possible particle hardening effect of undissolved carbides, although alternative explanations[1] suggest a possible effect of residual stresses.

7. Conclusions

A new model for predicting austenite formation during LHT is proposed. Novel features of the model include the implementation of the pearlitic nodule size and the interlamellar spacing as input parameters and a coupled treatment of the dissolution of cementite and formation of austenite. The model was validated with laser heat treatment experiments in AISI 1095. The main results can be summarized as follows: 1) The depth variation of austenite fraction, that is, the thickness of the hardened region correlates with both the reciprocal of the pearlitic noodule radius and interlamellar spacing. Small values of these variables produce fast formation of austenite, that is, a narrow transition and extended hardened regions. Conversely, larger values of pearlitic nodule radius or interlamellar spacing result in a narrower fully hardened layer and a thicker intercritical layer. 2) The rate of cementite dissolution decreases with the pearlitic nodule radius for a constant interlamellar spacing. 3) The fraction of transformed austenite decreases with the interlamellar spacing for a constant pearlitic nodule radius. 4) The hardness predictions of Equation (7) correlate well with the experimental measurements in terms of the extent of hardened layer and transition zone. The parameters that deliver the best fit are a pearlitic nodule radius 30 μm and interlamellar spacing of 0.1 μm. 5) The present set of results suggest that the formation of austenite in laser heat treatment experiments occurs with negligible superheating.

Acknowledgements

F.C.C. gratefully acknowledges the support of the National Agency for Research and Development (ANID-Chile), grant Fondecyt Regular No. 1220058.

Conflict of Interest

The authors declare no conflict of interest.

Author Contributions

Felipe Castro Cerda: conceptualization (equal); investigation (lead); writing original draft (lead). **Estefanía Sepúlveda**: formal analysis (equal); investigation (equal). **Leo Kestens**: formal analysis (equal); investigation (equal); writing—review and editing (equal). **Gentry Wood**: conceptualization (supporting); methodology (equal); resources (lead); writing—review and editing (equal). **Patricio Méndez**: conceptualization (equal); formal analysis (equal); writing—original draft (supporting); writing—review and editing (equal).

Data Availability Statement

The data that support the findings of this study are available on request from the corresponding author. The data are not publicly available due to privacy or ethical restrictions.

Keywords

austenite, hardness, laser heat treatment, modelling, pearlite

Received: July 18, 2025
Revised: November 21, 2025
Published online:

[1] J. Mazumder, *JOM* **1983**, *35*, 18.
[2] M. Bamberger, *Int. Mater. Rev.* **1998**, *43*, 189.
[3] J. Dutta Majumdar, I. Manna, *Int. Mater. Rev.* **2011**, *56*, 341.
[4] P. Dinesh Babu, K. Balasubramanian, G. Buvanashekaran, *Int. J. Surf. Sci. Eng.* **2011**, *5*, 131, pMID: 41398.
[5] J. Wang, J. Xia, Z. Liu, L. Xu, J. Liu, Y. Xiao, J. Gao, H. Ru, J. Jiao, *Int. J. Adv. Manuf. Technol.* **2024**, *134*, 5087.
[6] O. Kapustynskyi, N. Višniakov, *Photonics* **2025**, *12*, 207, Última actualización - 2025-03-27.
[7] S. Martínez, D. Lesyk, A. Lamikiz, E. Ukar, V. Dzhemelinsky, *Physics Procedia* **2016**, *83*, 1357, laser Assisted Net Shape Engineering 9 International Conference on Photonic Technologies Proceedings of the LANE 2016 September 19-22, 2016 Fürth, Germany.
[8] M. Ashby, K. Easterling, *Acta Metall.* **1984**, *32*, 1935.
[9] T. Chen, Y. Guan, H. Wang, J. Zhang, *J. Mater. Process. Technol.* **1997**, *63*, 546.
[10] R. Patwa, Y. C. Shin, *Int. J. Mach. Tools Manuf.* **2007**, *47*, 307.
[11] S. Skvarenina, Y. C. Shin, *Surf. Coat. Technol.* **2006**, *201*, 2256.
[12] *High Energy/Average Power Lasers and Intense Beam Applications* vol. *6454*, (Eds: G. Tani, L. Orazi, A. Fortunato, G. Campana, G. Cuccolini, In S. J. Davis, M. C. Heaven, J. T. Schriempf), International Society for Optics and Photonics, SPIE **2007**, p. 645404.
[13] L. Orazi, A. Fortunato, G. Cuccolini, G. Tani, *Appl. Surf. Sci.* **2010**, *256*, 1913.
[14] H. Yeo, M. Son, H. Ki, *Int. J. Heat Mass Transfer* **2022**, *197*, 123366.
[15] F. M. Castro Cerda, C. Goulas, D. Jones, A. Kamyabi, D. Hamre, P. Méndez, G. Wood, *Mater. Sci. Technol.* **2023**, *39*, 3123.
[16] D. Yu, T. Zhou, H. Zhou, P. Zhang, Y. Yan, *J. Mater. Eng. Perform.* **2022**, *31*, 3962.
[17] N. Zárubová, V. Kraus, J. Čermák, *J. Mater. Sci.* **1992**, *27*, 3487.
[18] A. Fernández-Vicente, M. Pellizzari, J. Arias, *J. Mater. Process. Technol.* **2012**, *212*, 989.
[19] F. Qiu, J. Uusitalo, V. Kujanpää, *Surf. Eng.* **2013**, *29*, 34.
[20] A. Bendoumi, N. Makuch, R. Chegroune, M. Kulka, M. Keddam, P. Dziarski, D. Przestacki, *Surf. Coat. Technol.* **2020**, *387*, 125541.
[21] M. N. M. Salleh, M. Ishak, M. H. Aiman, Q. Zaifuddin, M. M. Quazi, in *IOP Conference Series: Materials Science and Engineering*, Vol. *788*, IOP Publishing **2020**, p. 012014.
[22] Y. Lu, L. C. Ehle, S. Richter, T. Radel, *Surf. Coat. Technol.* **2021**, *421*, 127434.

[23] W. Charee, V. Tangwarodomnukun, *Opt. Laser Technol.* **2019**, *115*, 109.
[24] F. M. Castro Cerda, C. Goulas, D. Jones, A. Kamyabi, D. Hamre, P. Méndez, G. Wood, *J. Manuf. Processes* **2024**, *125*, 364.
[25] F. Castro Cerda, I. Sabirov, C. Goulas, J. Sietsma, A. Monsalve, R. Petrov, *Mater. Des.* **2017**, *116*, 448.
[26] G. Roberts, R. Mehl, *Trans. Asm* **1943**, *31*, 613.
[27] C. Zener, *J. Appl. Phys.* **1949**, *20*, 950.
[28] D. De Knijf, R. Petrov, C. Föjer, L. A. Kestens, *Mater. Sci. Eng.: A* **2014**, *615*, 107.
[29] P. Molian, *Mater. Sci. Eng.* **1983**, *58*, 175.
[30] W.-B. Li, K. E. Easterling, M. Ashby, *Acta Metall.* **1986**, *34*, 1533.
[31] P. F. Mendez, in *IOP Conference Series: Materials Science and Engineering* Vol. *1281*, IOP Publishing **2023**, p. 012021.